Korean J. Chem. Eng., 37(3), 434-447 (2020)
DOI: 10.1007/s11814-019-0455-z

pISSN: 0256-1115
eISSN: 1975-7220

Efficient treatment of anthraquinone dye wastewater by adsorption using sunflower torus-like magnesium hydroxide microspheres

Demin Jiang*, Fang Wang*, Bo Lan*, Dacai Wang*, Kezhong Liang*, Tingzhen Li*, Dongfeng Zhao*, Jianjun Chen**, Junjie Lin*,†, Wen Chan*, and Yuke Li***

*Key Laboratory of Water Environment Evolution and Pollution Control in Three Gorges Reservoir, Chongqing Three Gorges University, Chongqing 404100, China
**School of Chemical Engineering, Sichuan University, Chengdu 610065, China
***Chongqing Wanzhou District Ecological Environment Monitoring Station, Chongqing 404100, China
(*Received 17 July 2019 • accepted 7 December 2019*)

Abstract−Novel sunflower torus-like magnesium hydroxide (MH) microsphere particles were prepared by a facile one-step, self-assembly method. The synthesized products and the mechanism of adsorption of samples of the anthraquinone dyes reactive blue 19 (RB19) and alizarin red S (ARS) were analyzed by different modern characterization techniques, such as X-ray diffractometry (XRD), scanning electron microscopy (SEM), X-ray photoelectron spectroscopy (XPS), energy dispersive X-ray spectrometry (EDS), the Brunauer-Emmett-Teller (BET) method and Fourier transform infrared (FT-IR) spectroscopy. The adsorptive potential of the as-prepared microspheres for the removal of RB19 and ARS in aqueous solution was evaluated. The effects of multiple condition parameters, including, adsorbent dosage, adsorption time, adsorption temperature, wastewater pH, rotating speed and sodium chloride concentration on the removal of the dyes from the wastewater were studied in detail. The effect of the structural and shape properties of the MH adsorbent on the dye adsorption performances was also studied. The results showed that sunflower torus-like MH was an effective adsorbent for dye removal. The removal rates of ARS and RB19 were 91.65% and 83.03%, respectively, under the optimized conditions. The maximum adsorption capacity of the microspheres was 349.85 mg/g for ARS and 231.78 mg/g for RB19 at 25 °C. The equilibrium adsorption experimental data of the microsphere adsorption conformed to the Freundlich isotherm for ARS and the Langmuir isotherm for RB19. The adsorption kinetics experimental studies showed that the pseudo-second-order and pseudo-first-order model perfectly fit for both ARS and RB19 microsphere adsorption. RB19 and ARS were absorbed on the sunflower torus-like MH surface via the formation of H-bonds. Thus, the sunflower torus-like MH microsphere particles are an effective purifying agent for the removal of the anthraquinone dyes ARS and RB19 from wastewater.

Keywords: Synthesis, Sunflower Torus-like, Magnesium Hydroxide, Adsorption, Reactive Blue 19, Alizarin Red S

INTRODUCTION

Wastewater from the textile, paint, leather, printing, pigments, cosmetics, rubber, food, plastic and pharmaceutical industries usually contains residual toxic dyes [1-8]. In the past few decades, these residual dyes seriously affected water pollution once these harmful dyes flowed into the natural environment during the discharge of industrial wastewater. Worldwide, 10% of the 1×10^4 tons of synthesized dyes are emitted into the environment every year [9]. Several types of synthetic dyes are toxic and nondegradable pollutants. The model pollutants are anthraquinone dyes, which usually include a variety of highly carcinogenic, teratogenic and mutagenic aromatic functional groups [10]. As the second largest group consumed, anthraquinone dyes are widely used as primary dyes in commercial multicolor dyeing formulations for cotton fiber, wool and cellulosic fabric to produce satisfactory colors [11,12]. Once the anthraquinone dyes are discharged into the natural water environment, they not only impair the environmental water quality but also cause several health problems, including skin irritation, dermatitis, cancer and reproductive system issues in humans [13-15]. To provide a healthy and comfortable human living environment, these polluted waters must be treated in different ways for dye removal. Various methods have been tested to purify the harmful dyes from wastewater, including membrane separation [16], flocculation technology [17], electrochemical treatments [18], oxidation [19,20], adsorption [21-23], biodegradation [24,25], photocatalytic degradation [26,27] and Fenton's oxidation [28]. With a stable and unbreakable molecular structure, anthraquinone dyes are difficult to remove in wastewater treatment. Among these purification methods, adsorption is most suitable for treating wastewater, featuring a simple process, low energy consumption and satisfactory removal efficiency. The characteristics of the adsorbent usually play a very important role in the purification process. Thus, the synthesis and application of high-efficiency adsorbents are crucial for the industrialization of adsorption methods. To date, various adsorbents have been prepared for removing dyes from polluted water, such as clays [29,30], activated carbon [31,32], biochar [33], chitosan [34], graphene and graphene oxide [23,35], polymer mate-

†To whom correspondence should be addressed.
E-mail: ybu_lin@126.com

rials [36], metal oxides and hydroxides [37-39]. Although activated carbon, chitosan, graphene and graphene oxide have been extensively used in dye wastewater treatment, the complicated preparation processes and high cost remain obstacles in their industrial manufacture. Therefore, low-cost and easily obtained adsorbents are utilized for the adsorption of dyes. MH has been intensively researched for its wide application in various fields [40-43]. MH seems to have prospects and is highly recommended for removing dye contaminants [44,45]. Due to the low specific surface area and filtration difficulty, the application of magnesium hydroxide is currently limited. MH with an ultrafine nanoscale particles size has an efficient dye removal rate, but it is difficult to filter in wastewater treatment. Therefore, to solve this problem, it is essential to prepare micron-sized adsorbent particles with pore structures.

In this work, a novel microscale particle of sunflower torus-like magnesium hydroxide (MH) was successfully synthesized by a special method. Various modern detection technologies were employed to analyze the structures and shapes of this composite material, and the adsorption properties for the anthraquinone dyes RB19 and ARS on the surface of MH microsphere particles were comprehensively investigated.

EXPERIMENTAL METHODS

1. Chemicals

The raw materials magnesium sulfate heptahydrate, ammonia, caustic soda, ethanol, sodium chloride, hydrochloric acid, sodium dodecyl sulfate, reactive blue 19 (RB19) and alizarin red S (ARS) were used in the present work. The molecular structures of RB19 and ARS are shown in Fig. 1. RB19 was purchased from Jinan Longsheng Dyestuff Chemical Co., Ltd. (Jinan, China). ARS was produced by Shanghai Chemical Reagent Purchasing and Supply Station (Shanghai, China). The rest of the chemical reagents were purchased from Xilong Scientific Co., Ltd. (Sichuan, China). The RB19 and ARS dyes are of industrial grade purity, and the other reagents and materials used in this study were analytically pure (A.R. grade).

2. Synthesis

The sunflower torus-like MH microsphere particles were synthesized via the one-step, self-assembly method described in our previous work [46,47]. A certain amount of magnesium sulfate heptahydrate crystals and a certain quality crystal control agent, sodium dodecyl sulfate, were added to a 250 mL beaker with deionized water. The mixtures were stirred to dissolve and mixed well.

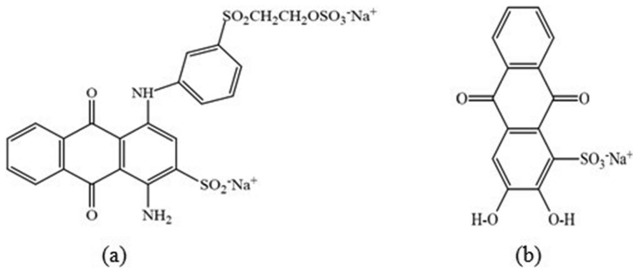

Fig. 1. The molecular structure of RB19 (a) and ARS (b).

Under vigorous stirring, caustic soda solutions were dropped into the solution. The beaker was closed in a container filled with ammonia solution, and the two solutions were kept out of contact. The device was statically placed at 25 °C to react for 24 h. A white product was obtained after filtration and washing several times. Then, the products were dried at 120 °C for 24 h after washing with ethanol.

3. Characterization

Several characterization methods were used to analyze the physicochemical properties of the white powder product. The elemental composition of the sunflower torus-like MH microsphere particles was determined by an energy dispersive X-ray spectrometer (EDS, Helois Nano Lab 600, USA). The microscopic morphologies were observed by the field emission scanning electron microscope (SEM, JSM-7500F, Japan). The Brunauer-Emmett-Teller (BET, autosorb-IQ2-MP-XR-VP, USA) surface area and porosity analyzer were employed to examine the microstructural parameters. The structures of samples were detected by an X-ray diffractometer (XRD, Bruker D8 advance, Germany). The Fourier transform infrared spectrum was recorded on a Fourier transform infrared spectrometer (FT-IR, Nicolet iS10, USA) in KBr disc. An X-ray photoelectron spectrometer (XPS, Escalab 250Xi, USA) was employed to identify the composition and chemical state of the elements on the surface of sunflower torus-like samples before and after treatment with a dye solution. The dye concentrations were analyzed with a spectrophotometer (V-1500, China) provided by Shanghai Macy Instrument Co., Ltd.

4. Adsorption Experiments

The adsorption experiments, which included the process optimization experiment, isothermal equilibrium experiment and kinetics experiment, were carried out as follows. The adsorbent powder and the dye solution were placed in a 100 mL stoppered conical flask. Then, the flask was placed in the constant temperature oscillation box (BS-1E, China) provided by Jintan Zhengji Instrument Co., Ltd. After the adsorption was completed, the mixed solution was poured into a centrifuge tube to separate the adsorbent and the solution with the centrifuge (KA-1000, China) provided by Shanghai Anting Scientific instrument factory. The dye concentration in solution was analyzed with the spectrophotometer.

Initially, various parameters, such as mixing time, the amount of sunflower torus-like MH microsphere particles added, adsorption temperature, wastewater pH, rotation speed and sodium chloride concentration, were optimized. The simulated anthraquinone dye wastewater concentration was 100 mg/L for RB19 and ARS solution. Adsorption experiments were studied by varying the amount of MH (0-80 mg), contact time (0-45 min), temperature (15-65 °C), pH (1.02-13.76), rotating speed (60-300 r/min) and with a varying amount of sodium chloride (0-0.5 mol/L). To determine the optimized process parameters, the conditions of MH microsphere particles for the anthraquinone dyes RB19 and ARS adsorption were investigated.

The isothermal equilibrium experiment and kinetics experiment were accomplished after the optimization of adsorption conditions. Then, the relevant performances were evaluated via the following models.

The adsorption capacity (Q_e, mg/g) was based on isothermal equi-

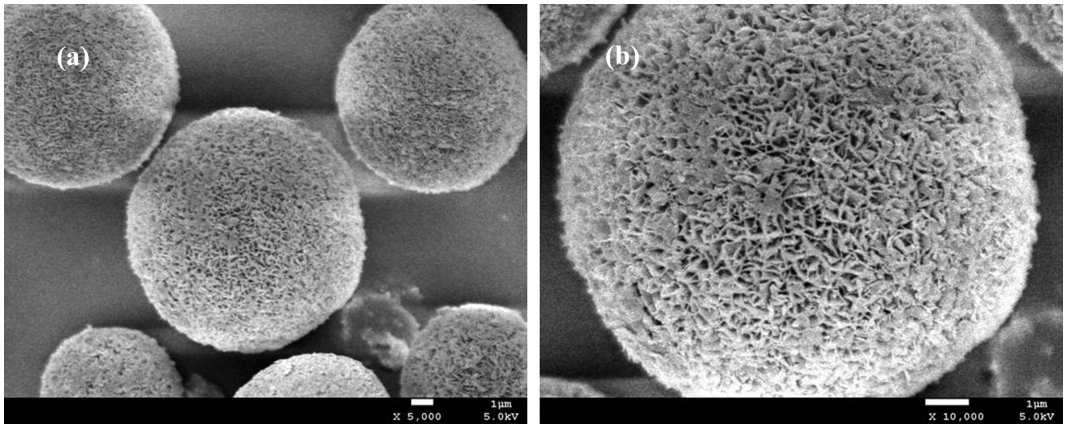

Fig. 2. SEM images of the Sunflower torus-like MH.

librium experiments studies, which were carried out under contact for 40 min. Moreover, the initial anthraquinone dye concentration was 50-1,000 mg/L. Therefore, the Langmuir equation (Eq. (1)) [48] and Freundlich equation (Eq. (2)) [49] were employed to assess the isothermal adsorption performance.

$$Q_e = \frac{Q_m K_L C_e}{1 + K_L C_e} \quad (1)$$

$$Q_e = K_F C_e^{1/n} \quad (2)$$

The removal rates for the treatment of dye wastewater with sunflower torus-like MH microsphere particles were investigated by the preceding kinetic model. For two types of dyes, the initial concentration (C_i) was 100 mg/L, and the contact time was implemented for 0-40 min at 25 °C. The adsorption kinetics experiments were evaluated by kinetic models of the pseudo-first-order (PFO) equation (Eq. (3)) and pseudo-second-order (PSO) equation (Eq. (4)) [8,50] in this work.

$$Q_t = Q_e(1 - e^{-k_1 t}) \quad (3)$$

$$Q_t = \frac{k_2 Q_e^2 t}{1 + k_2 Q_e t} \quad (4)$$

The dye concentrations (C_t, mg/L) of RB19 and ARS were determined by spectrophotometry after adsorption for a period of time. Eq. (5) was used to evaluate the adsorption rate (N_t). Eq. (6) was also adopted to estimate the adsorption capacity (Q_t).

$$N_t = \frac{C_0 - C_t}{C_0} \times 100\% \quad (5)$$

$$Q_t = \frac{C_0 - C_t}{m} V \quad (6)$$

Here, C_e (mg/L) is the adsorption equilibrium concentration. Q_m (mg/g) is the maximum amount of adsorption, and Q_e (mg/g) is the amount at the adsorption equilibrium. K_L (L/mg) and K_F, respectively, represent the balance factor and equilibrium constant. The parameter of n is the adsorption index in the Freundlich equation. The adsorption capacity at any time (t (min)) of the adsorption mixing process is Q_t (mg/g). Both k_1 (min^{-1}) and k_2 (g/mg·min) are rate constants for the PFO model and PSO model, respectively. The removal rate at any time (t (min)) during the adsorption process is N_t. C_0 (mg/L) and C_t (mg/L), respectively, represent the concentration values of adsorbed substances before and after the adsorption time of t (min). V (L) is the volume dye solution used. The m (mg) is the added weight of the sunflower torus-like MH microsphere particles.

RESULTS AND DISCUSSION

1. Characterization Analysis of Materials

The microscopic morphological structure of the as-synthesized novel MH particles was examined by SEM. Fig. 2 shows the dimensions and morphological structure of the synthesized products by this method. Fig. 2 shows that the particle is a microsphere with many holes on the surface, like the sunflower torus after removal of the seeds. At the same time, the lamellar and other irregular particles did not appear. The diameter of the microsphere particles was approximately 10 μm. As shown in Fig. 2(a), the morphology of this sample indicated that the particles presented a rough surface rather than being dense, smooth and spherical. Fig. 2(b) shows us

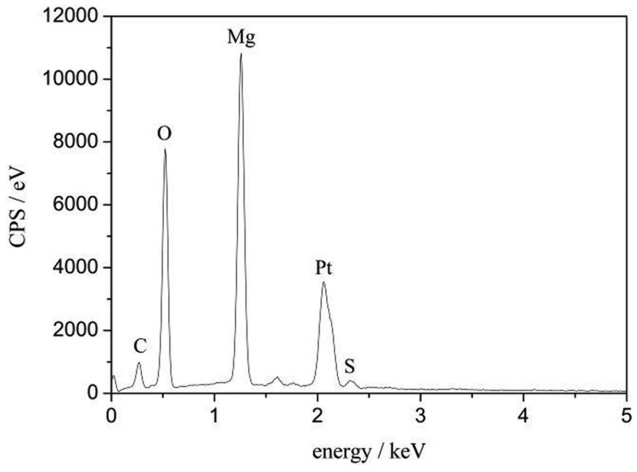

Fig. 3. EDS pattern of microsphere particles.

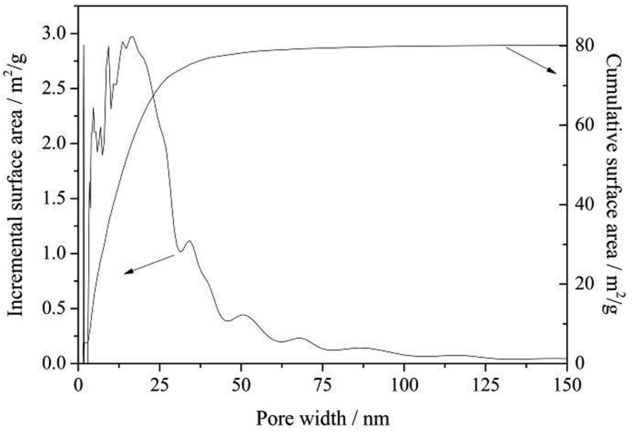

Fig. 4. Surface area of the aperture.

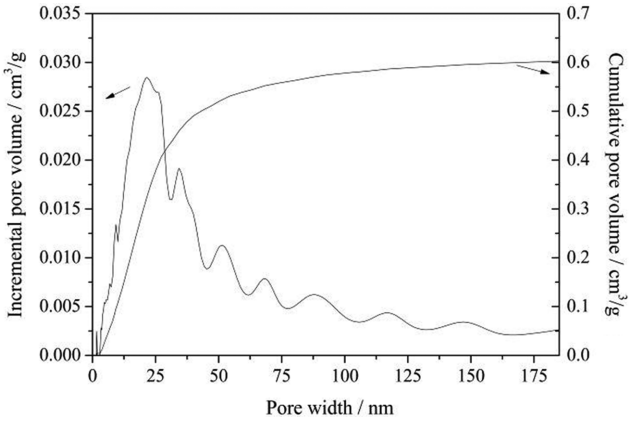

Fig. 5. Pore volume of aperture.

that the microsphere particles were formed by nanoflakes, and there are many slotted irregular holes on the surface.

EDS technology was used to further investigate and affirm the chemical composition on the surface of the microsphere particles. Five elements were assessed, as shown in Fig. 3. In the spectrum of Fig. 3, the strong Pt diffraction peak is from the gold sputtering process in EDS analysis. The detected elements C and S are due to the sodium dodecyl sulfate loaded on MH. Therefore, the microsphere sample only contains two elements, O and Mg, which further proved that the sunflower torus-like microsphere particles are pure MH.

The pore widths distributed between 2 nm and 50 nm are mainly mesoporous (Fig. 4 and Fig. 5). In addition, there are some macropores distributed between 50 nm and 180 nm. The cumulative mesoporous surface area is 80.2 m^2/g (Fig. 4). The cumulative mesopore surface area mainly comes from the 2 nm to 50 nm mesoporous surface. The mesopore with the average pore diameter of approximately 15.9 nm has the largest contribution to the surface area. The cumulative pore volume of the spherical product is 0.6 cm^3/g (Fig. 5). The pore volume mainly comes from mesopores distributed between 2 nm and 50 nm. The average pore diameter (4 V/A) is 17.7 nm according to BJH adsorption analysis.

The FT-IR spectrometer was also used to examine the functional groups. The FT-IR spectra of the sunflower torus-like MH before and after dyes were adsorbed are shown in Fig. 6. All the samples had strong peaks distributed at approximately 3,698 cm^{-1} and 3,438 cm^{-1}. After the adsorption of RB19 and ARS, the intensity of the characteristic hydrogen bond peak was enhanced, and the position changed from 3,436.24 cm^{-1} to 3,438.82 cm^{-1} and 3,438.13 cm^{-1}, respectively. The number of hydrogen bonds increased on the surface of samples after adsorbing dyes. The diffraction intensity of the H-O-H bending vibration feature peak was significantly changed. The position of the peak at 1,632.95 cm^{-1} was also changed to 1,630.96 cm^{-1} and 1,631.42 cm^{-1}. It was indicated that there were more coordinated water molecules on the samples. More importantly, there were many weak diffraction peaks appearing after absorption of the dyes. After treatment with RB19 solution, a weak peak emerged at 1,562 cm^{-1}, which can be labeled as the telescopic vibration of -NH_2 functional groups [51]. Some weak peaks at 1,504.27 cm^{-1} and 1,505.23 cm^{-1} corresponded to the C=C stretch vibration of the benzenoid ring and quinoid ring in the reactive blue 19 (RB19) and alizarin red S (ARS) [52,53]. The weak peak at 1,042.38 cm^{-1} was attributed to the S=O stretching vibration in the -SO_3^- group [53]. The results of the FT-IR spectra analysis show that the dye molecules were anchored onto the surface of the sunflower torus-like MH.

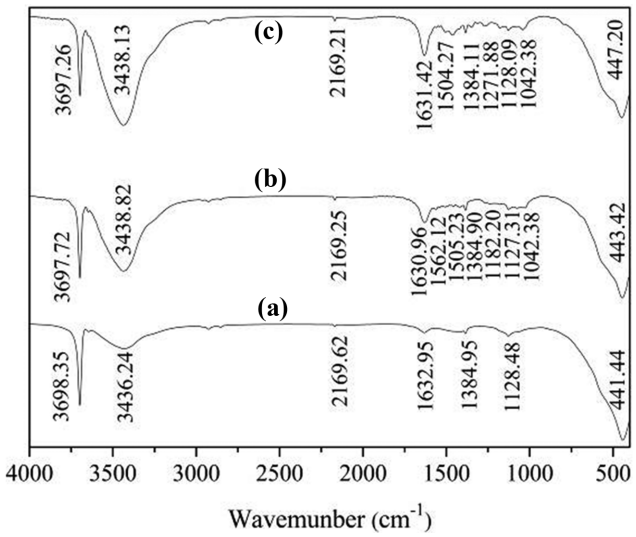

Fig. 6. FT-IR spectra of (a) MH, (b) MH with adsorbed RB19 and (c) MH with adsorbed ARS.

The X-ray diffractometer was used to study the internal structure of this sample. The XRD spectra of the sunflower torus-like sample and after adsorbing dyes are shown in Fig. 7. According to the standard spectra of JCPD 7-239, all the diffraction peaks of XRD spectra indicated that the as-synthesized sunflower torus-like sample was hexagonal-phase magnesium hydroxide (MH) in Fig. 7(a). The strongest and sharpest diffraction peak emerged in the (101) plane. Strong diffraction peaks also appeared on the (001), (102) and (110) planes. Weak diffraction peaks emerged in the (100), (111), (103) and (201) planes. Thus, there were no additional phase diffraction peaks in the XRD spectrum. It was shown that the as-synthesized sunflower torus-like sample was high purity MH. After

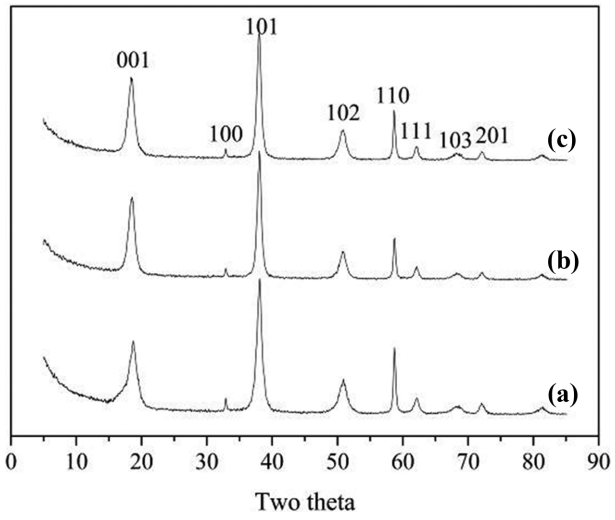

Fig. 7. XRD spectra of (a) MH, (b) MH with adsorbed RB19 and (c) MH with adsorbed ARS.

treatment with dye molecules, the intensity of the diffraction peaks at the (001) and (110) planes was obviously enhanced, and the other diffraction peak intensities showed no significant change. Therefore, no new diffraction peak was detected for the adsorbed particles in Fig. 7(b), (c).

To verify the existence of the dye molecule, the composition and chemical state of the elements on the surface of sunflower torus-like microsphere samples before and after treatment with dye solution (1,000 mg/L) was tested via XPS measurements, as shown in Fig. 8. The survey scanning XPS spectra indicated that the elements before and after treatment with the dye solution are mainly Mg, O, C and S. Fig. 8 shows that strong peaks that emerged at 531 eV (O 1s) and 1,304 eV (Mg 1s) had no significant change after treatment with the dye solution (1,000 mg/L). However, the diffraction peak intensity of C 1s at 285 eV was significantly enhanced after

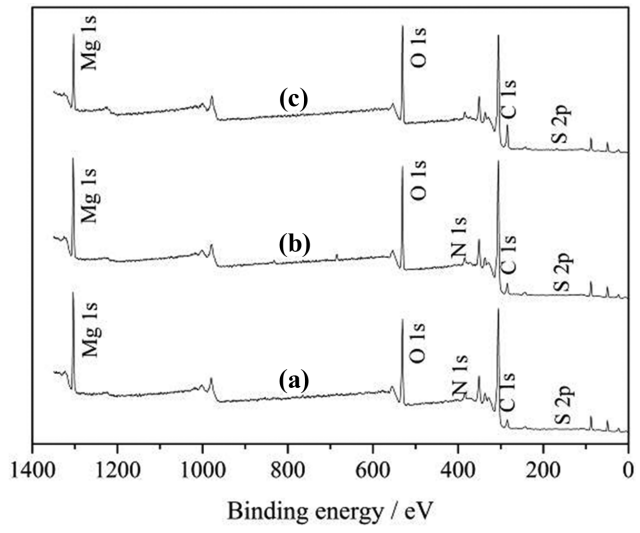

Fig. 8. XPS spectra of (a) MH, (b) MH with adsorbed RB19 and (c) MH with adsorbed ARS.

Table 1. Atomic contents of (a) MH, (b) MH with adsorbed RB19 and (c) MH with adsorbed ARS

Specimen	Atomic content/%					
	Mg 1s	O 1s	C 1s	S 2p	N 1s	Na 1s
a	30.53	54.30	14.27	0.32	0.48	0.10
b	30.04	54.14	15.01	0.27	0.45	0.09
c	19.11	48.11	31.60	0.96	0	0.21

adsorbing ARS. It was indicated that the dyes were present on the sunflower torus-like microsphere particles. The atomic ratios of the surface elements before and after sample treatment with dye solution are shown as in Table 1, where the atomic ratio exhibits no significant change after absorbing the RB19 dye. However, the atomic ratio of the sunflower torus-like microsphere sample treated with the ARS solution obviously changed. In particular, the atomic ratio of Mg 1s decreased from 30.53% to 19.11%, and that of C 1s increased from 14.27% to 31.60%.

To further determine the elemental valence states of the samples, the high-resolution XPS spectrum was also used to analyze the absorption spectrum of each element. The high-resolution XPS spectra of the detected elements are shown in Fig. 9. From the high-resolution spectrum of Mg 1s, we can see that there were two peaks located at the binding energies of 1,304.13 eV and 1,303.91 eV for the sunflower torus-like microsphere MH. This result indicates that there was only a valence state and two chemical states present for the magnesium atom. After treatment with the RB19 dye solution, another new peak emerged and was located at the binding energy of 1,304.96 eV. This result indicates that a new chemical state was present for the magnesium atom. However, after treatment with the ARS dye solution, the two peaks were shifted to 1,303.86 eV and 1,303.54 eV, respectively. The analysis of the Mg 1s spectrum indicates that dyes were present on the sunflower torus-like microsphere sample. The C 1s photoelectron peaks of the three samples were all decomposed into five symmetrical peaks. A weak peak emerged at approximately 290.00 eV in the peak fitting spectrum that was attributed to the $\pi \rightarrow \pi^*$ shake-up of the sp^2-hybridized carbon atoms [54]. The satellite peak was enhanced after treatment with dye solution. The symmetrical peaks at approximately 288.76 eV and 285.84 eV were assigned to C-O- and COO- groups, respectively [55,56]. The fitting peak that emerged at approximately 284.67 eV was due to the C-C/C=C groups [57]. The positions of all fitting peaks were changed, and the peak intensity of the fitting at 284.71 eV was significantly enhanced after the dye was adsorbed on the surface of the sunflower torus-like sample. From the high-resolution O 1s spectrum, the photoelectron peak of the MH sample was decomposed into four symmetrical peaks. The fitting peak at 534.39 eV was assigned to the presence of $MgCO_3$ [58]. This peak may be attributed to CO_2 from the air adsorbing on the surface of the MH sample and forming $MgCO_3$. The characteristic peak of $MgCO_3$ disappeared after the dye was adsorbed on the surface of the sunflower torus-like sample. The other three peaks at 532.84 eV, 531.74 eV and 530.71 eV can be marked as the C-OH functional group, Mg-O bond and lattice oxygen, respectively [57,58]. After adsorption of the RBB19 and ARS

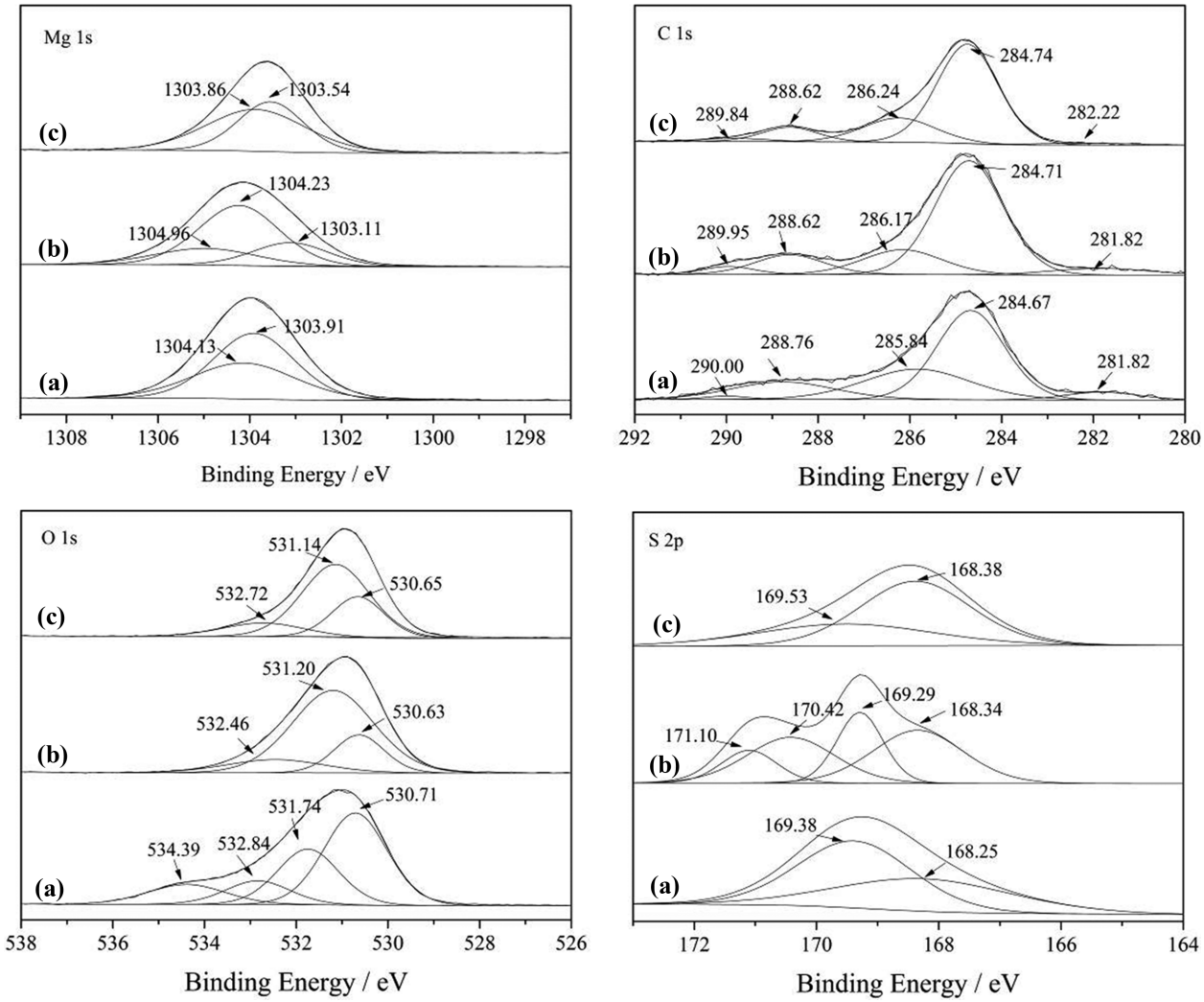

Fig. 9. High resolution XPS spectra of Mg 1s, C 1s, O 1s and S 2p ((a) MH, (b) MH with adsorbed RB19 and (c) MH with adsorbed ARS).

dyes, the intensity of the peaks increased, and the binding energies were shifted from 531.74 eV to 531.20 and 531.14 eV, respectively. The high-resolution S 2p spectrum of MH exhibits a peak at 169.38 eV that was assigned to the four oxygen atoms located in the first neighborhood [59]. It may be the interfacial SO_4^{2-} that was absorbed on the sample surface [60]. The peak at 168.25 eV was assigned to two oxygens doubly bonded and one singly bonded oxygen to a sulfur atom as a -SO_3H group [59]. The intensity of the fitting peak was significantly enhanced after treatment with ARS solution, which was because the -SO_3H group existed in the ARS molecule. Two other new peaks at 171.10 eV and 170.42 eV emerged after the adsorption of RB19.

2. Parameter Optimization of Sunflower Torus-like Microsphere MH Adsorption Dyes

In the process of the adsorption treatment of harmful substances, the adsorption rate and capacity are highly dependent on the adsorption process parameters. Thus, the effects of the adsorption process parameters were investigated in detail and are discussed as follows.

2-1. Adsorbent Dosage

A suitable amount of adsorbent plays an important role in the adsorption experiments. The amount of adsorbent determines the ability of the adsorbent to treat the particular initial dye concentration in a solution. To prevent the adsorbent from being wasted and to maximize the adsorption efficiency, optimizing the amount of sunflower torus-like MH microsphere particles is indispensable.

A volume of 15 mL of 100 mg/L anthraquinone RB19 and ARS dye solutions was tested by altering the amount of MH spherical products between 0 and 80 mg with other conditions fixed as follows: adsorption time of 160 min, adsorption speed of 200 r/min and adsorption temperature of 20 °C. The dye removal rates with respect to MH microsphere products dose are shown in Fig. 10. The maximum removal rates were 84.52% and 95.29% for dye wastewater samples with RB19 and ARS, respectively, with the adsorbent dose of 80 mg. Initially, the dye removal efficiency for the microsphere particles adsorption RB19 and ARS changed sharply as the amount of microsphere particles varied from 5 to 25 mg and from 5 to 40 mg. This result occurred because adsorption active sites were increased with the increasing amount of adsorbent. When continuing to increase the amount of adsorbent, the removal rate of the dye in wastewater no longer changed. The

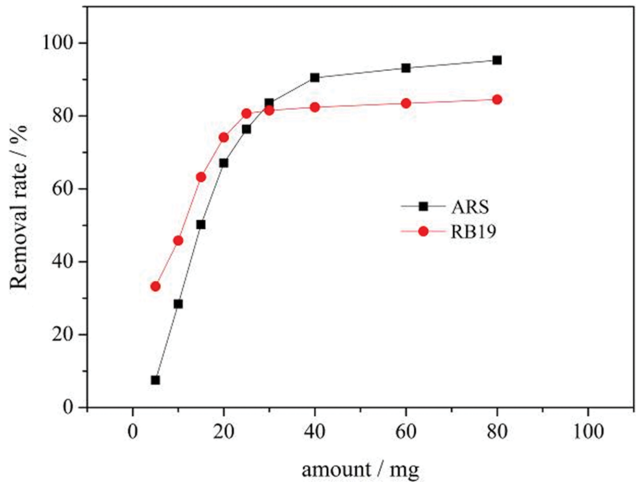

Fig. 10. Effect of the adsorbent amount on the removal rates of ARS and RB19.

optimum adsorbent amount was found to be 25.0 mg for RB19 solution, which yielded 80.69% removal efficiency, and 40 mg for ARS solution, which yielded 90.48% removal efficiency. Doses of 25 mg and 40 mg of MH microsphere products were used for the adsorption of RB19 and ARS wastewater samples, respectively, for maximizing the utilization rate of microsphere particles. After the successful optimization, all RB19 adsorption experiments were performed with 25 mg of the adsorbent MH, and 40 mg of the microsphere products was used in ARS wastewater purification experiments.

2-2. Contact Time

According to the literature reports, contact time is a valuable parameter in the adsorption study [61]. A certain time is necessary to complete the adsorption process with various adsorbents. The effect of adsorption time on the MH uptake of anthraquinone dye was investigated. Additionally, the removal rates of RB19 and ARS are shown in Fig. 11. The initial concentration of all dyes was 100 mg/L, and the amount of MH was the optimum value. Initially, the removal efficiencies of the two dyes increased sharply with the contact time extension. Moreover, in the same contact time, the removal rate of ARS was higher than that of RB19. After 20 min, the removal rate of ARS was maintained when the contact time was further extended; the available surface sites were nearly occupied. However, the removal rate of RB19 continued to increase in the next 10 min. It took 30 min for that removal rate to reach a constant in the adsorption RB19 experiments. Vacant sites were not available for dye adsorption, and the adsorption process was saturated. Thence, no additional dyes were detected, adsorbed and removed as time went on. It may be concluded that, for RB19 and ARS, the optimized contact times are 20 min and 30 min, respectively. The maximized percentage removal rate and adsorption capacity were achieved in the optimization of contact time. Therefore, the contact time of all RB19 wastewater purification experiments was performed for 30 min, and 20 min was adopted for ARS adsorption experiments.

2-3. Temperature

The temperature can change the movement speed of the adsorbed material in the solution. Therefore, temperature is an important parameter in wastewater treatment by the adsorption method [62]. The removal rates of RB19 and ARS by MH adsorption with changing temperature are shown in Fig. 12. As expected in this study, increasing the adsorption temperature can increase the removal rate. However, the removal rate does not significantly change. For ARS adsorption experiments, the removal rate gradually increased from 86.02% to 93.03% as the adsorption temperature changed from 15 °C to 45 °C. The removal rate of RB19 changed from 73.24% to 84.61% in the same temperature range. The adsorption effects were increased with increasing adsorption temperature. It indicated that MH adsorption of ARS and RB19 are endothermic reactions. The elevated temperature enhances the kinetic activity of the dye molecules, thus promoting more dye molecules to penetrate the internal voids of the microsphere product. At higher adsorption temperatures, the removal efficiency of the two dyes remained essentially unchanged. Fig. 12 shows that the optimal adsorption temperature is 55 °C. Although increasing the temperature can improve the purification effect, the changes for the two samples were not significant. Thus, it is recommended

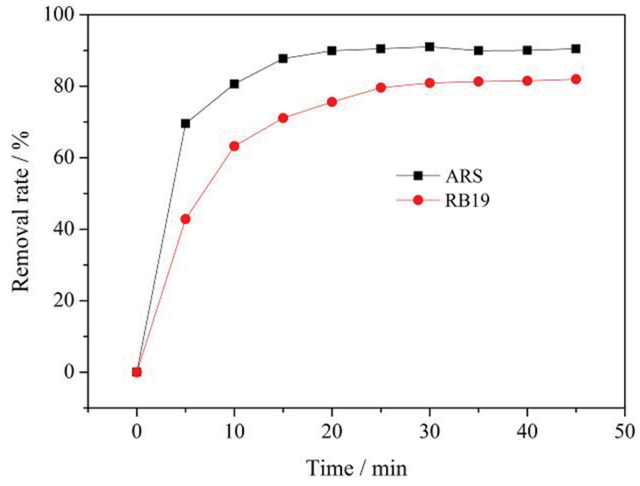

Fig. 11. Effect of contact time on the removal rate of ARS and RB19.

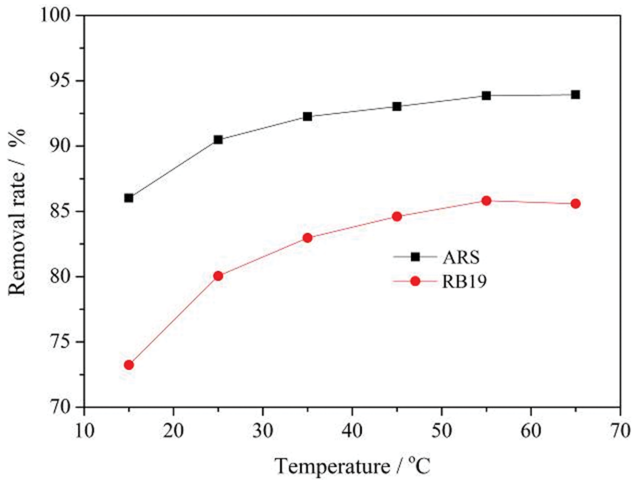

Fig. 12. Effect of temperature on the removal rate of ARS and RB19.

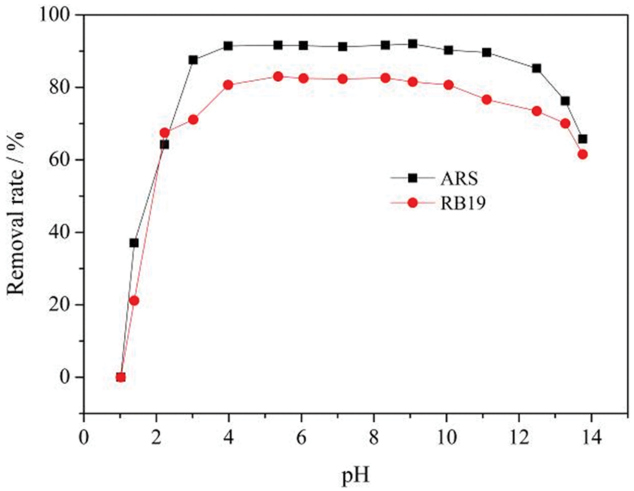

Fig. 13. Effect of pH values on the removal rates of ARS and RB19.

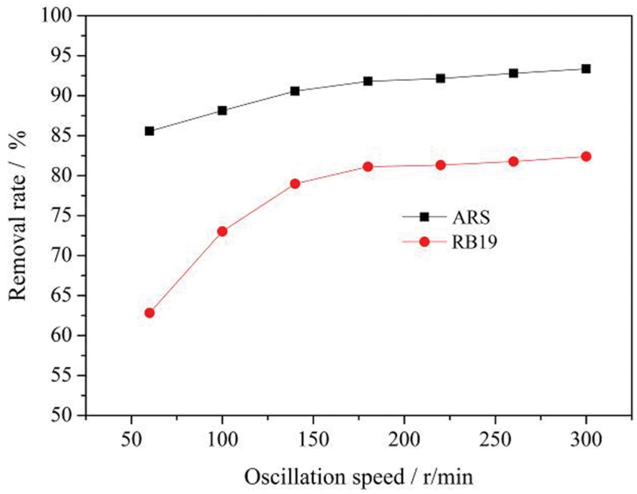

Fig. 14. Effect of oscillation speed on the removal rates of ARS and RB19.

that room temperature is selected as adsorption temperature.

2-4. Initial Dye Solution pH

The effect of the pH of the dye solution on the dye adsorption performance and, hence, on the removal efficiency was tested by varying the pH of the dye solution. Sodium hydroxide and hydrochloric acid were used to regulate the pH values of the dye solutions. The required amount of hydrochloric acid (or sodium hydroxide) was added to the dye solution when configuring the 100 mg/L dye solution. Then, the pH values of dye solutions were determined by a pH meter before adsorption. Fig. 13 shows the removal rate at different initial pH values of dye wastewater. The initial dye solutions pH values were changed from 1.02 to 13.76. The dye removal efficiency changed drastically when pH values increased from 1.02 to 3.98 (Fig. 13). Under the strongly acidic environment, the adsorption processes of RB19 and ARS both showed the worst removal efficiency of 0.00% at pH 1.02. During the experimental process, we found that the MH samples disappeared with the high initial acidity of the dye solution. The lower the initial pH of the dye solution was, the more the adsorbent sample was dissolved. The active sites of carrier adsorption dye molecules were decreased with decreasing pH values. Thus, the acidity of the solution had a significant effect on the removal of the dye when the solution pH was between 1.02 and 3.98. The removal rates were significantly increased by increasing the pH values from 1.02 to 3.98. The efficiency data were insignificantly changed for both the samples at pH values of 3.98-10.06. Better removal efficiency was observed with a maximum of 91.65% and 83.03% for the ARS and RB19 dye wastewater samples, respectively. At higher pH values, MH attraction to dye molecule was impeded by various hydroxyl ions attached to the sunflower torus-like MH microsphere materials surface. Hence, the removal efficiency began to decrease for both dye wastewater samples as the pH values further increased. The solution pH range of 4 to 10 was easy to control for the adsorption of dyes in industrial production. Finally, adsorption tests were performed at solution pH values of 4 to 10.

2-5. Rotating Speed

The effect of oscillation speed on the dye removal efficiency was tested by varying the oscillation speed in the experiment. Fig. 14 shows the removal rate in this method. The effect of the oscillating speed on the MH microsphere particle adsorption of ARS was higher than that for the MH adsorption of RB19 (Fig. 14). Initially, the dye removal rate increased sharply when the oscillation speed of the RB19 solution increased from 60 to 180 r/min. That result because the rate of the dye molecule mass transfer increased in the solution. Then, the removal rate of RB19 no longer changed with the increase in the oscillation speed in the experiment. However, for the ARS adsorption experiments, the percentage removal rate gradually changed when the adsorption speed increased. This study showed that the process of MH surface adsorption controlled the rate of adsorption in the ARS experiments. The rate of dye molecule transfer in solution was the controlling step of MH adsorption of RB19 at low speed. Thus, it is advised that the adsorption experiments be performed at the oscillation speed of 180 r/min in industrial production.

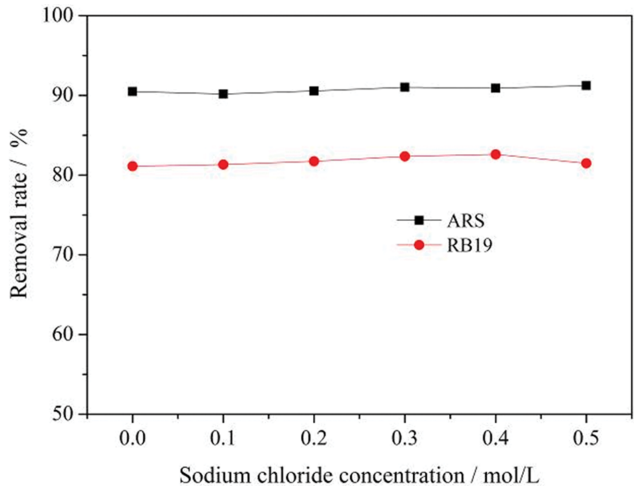

Fig. 15. Effect of sodium chloride on the removal rates of ARS and RB19.

2-6. Concentration of Sodium Chloride

According to the reported literature, there is substantial sodium chloride in dye wastewater. This high concentration may have an impact on the temperature of the adsorption process. Different sodium chloride concentrations from 0.0 to 0.5 mol/L were used in the dye solution. The initial concentrations of both dyes were 100 mg/L, and all other parameters were the optimum values. As the concentration of sodium chloride increased, the removal efficiency remained constant for both samples, as shown in Fig. 15. This result indicates that sodium chloride does not affect MH adsorption of the RB19 and ARS dyes.

3. Adsorption Efficiency of Different Shapes MH

The adsorption efficiency of the manganese dioxide removal of thallium from wastewater was significantly affected by the morphology and shape of the adsorbent [63]. To explore the effect of the structural and shape properties of the MH adsorbent on the dye adsorption performances, various morphologies were applied for the removal of dye from wastewater and compared with the adsorption efficiency of sunflower torus-like MH. The hydrothermal method [64]-hydrothermal conversion [65] and precipitation method [66] were employed to synthesize whisker-shaped and lump-shaped MH, respectively. Adsorption experiments were performed at the optimized conditions for the sunflower torus-like MH adsorption of dyes: the MH amount (25 mg for RB19 and 40 mg for ARS), contact time (30 min for RB19 and 20 min for ARS), adsorption temperature (25 °C), dye solution pH (4-10) and rotating speed (180 r/min). The effect of various shapes of MH particles on dye adsorption efficiency is shown in Table 2. Table 2 shows that the dyes removal rate was significantly affected by the morphology of the MH. Among the following three shapes, the removal rate of sunflower torus-like MH was highest. The removal rates were increased by at least 33.35% and 31.47% for ARS and RB19. It indicated that the dye adsorption performances were affected by the structural and shape properties of MH. The specific surface area of sunflower torus-like MH was the highest of the three samples with varied shapes. With many large pores and mesopores of the sunflower torus-like MH, more surface sites were provided for dye adsorption. Therefore, the adsorption of dyes on sunflower torus-like MH showed excellent adsorption efficiency.

4. Adsorption Isotherms

The characteristics of the adsorption equilibrium of sunflower torus-like MH microsphere particle materials adsorbing RB19 and ARS were analyzed by the equilibrium adsorption isotherm model. The isothermal adsorption parameters were calculated from the experimental plots via the previous equations (Eq. (1) and Eq. (2)). These parameters are listed in Table 3, and the isothermal balance lines are presented in Fig. 16.

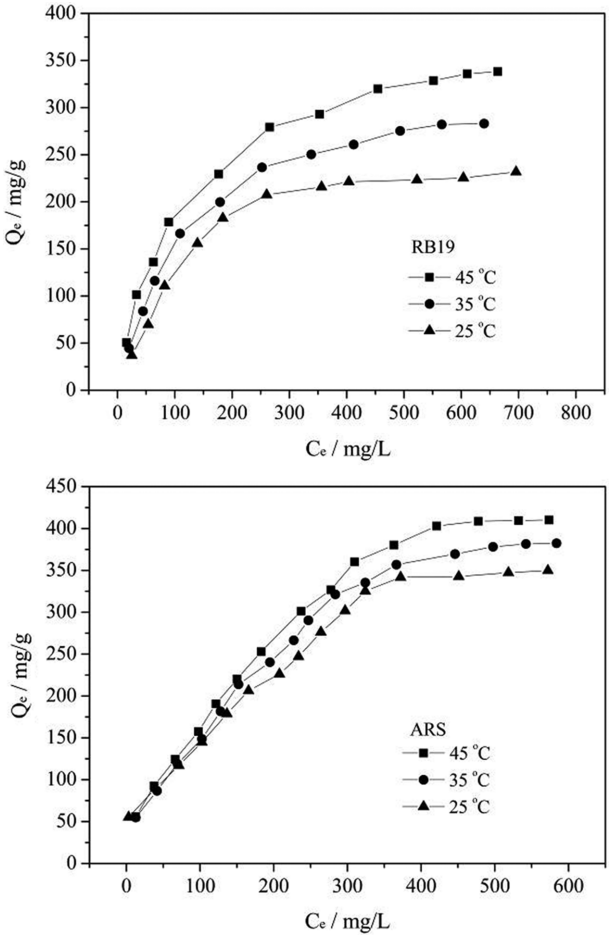

Fig. 16. Isothermal adsorption curve.

Fig. 16 shows that the capacity of saturated adsorption was affected by temperature change. Initially, the saturated capacity of MH adsorption of RB19 increased sharply when the balanced concentration of RB19 solution changed from 15 to 260 mg/L. Correspondingly, the adsorption capacity of MH adsorption of ARS gradually changed when the balanced concentration of ARS increased from 3 to 370 mg/L. With the same conditions, the saturated capacity of MH adsorption of ARS blue also increased with increasing temperature. However, there was an insignificant effect at lower equilibrium concentrations. Under the same experimental conditions, the saturated capacity of the MH adsorption of ARS was higher than that of RB19. The increasing temperature led to

Table 2. Effect of various shapes of MH particles on the removal rate

Parameters	Shape of MH samples		
	Whisker-shaped	Lump-shaped	Sunflower torus-like*
Specific surface area (m^2/g)	23.15	61.40	98.04
Removal rate of RB19 (%)	36.31	50.01	81.48
Removal rate of ARS (%)	53.11	57.88	91.23

Note: * this study.

Table 3. Isothermal adsorption parameters

Dyes	T (°C)	q_m (mg/g)	Langmuir			Freundlich		
			K_L (L/mg)	Q_m (mg/g)	R^2	K_F	n	R^2
ARS	25	349.85	0.102	223.71	0.7166	26.29	2.45	0.9192
	35	382.41	0.0147	322.58	0.8926	12.13	1.78	0.9799
	45	410.21	0.0135	354.61	0.9221	12.33	1.75	0.9867
RB19	25	231.78	0.00475	352.11	0.9923	9.20	1.90	0.8872
	35	283.04	0.00693	362.32	0.9988	9.35	1.75	0.8952
	45	338.24	0.00964	386.10	0.9955	17.94	2.12	0.9501

more intense irregular movements of dye molecules, which caused more dye molecules to penetrate the internal voids of mesoporous spherical products, resulting in the high saturated adsorption capacity.

Based on Table 3, the isotherms of sunflower torus-like MH microsphere particles adsorption ARS were well-fitted in the Freundlich equation at three different experimental temperatures (correlation coefficient: $R^2_{Freundlich}>R^2_{Langmuir}$). However, the Langmuir model was the appropriate candidate to describe the RB19 adsorbed on MH (correlation coefficient: $R^2_{Langmuir}>R^2_{Freundlich}$). The results showed that the process of sunflower torus-like MH adsorption of RB19 was probably completed by single molecule adsorption. The index n of the Freundlich equation also stipulated the favorability of the adsorption process [67]. The exponent n values changed from 2.45 to 1.75 for ARS and from 1.90 to 2.12 for RB19 when temperature increased from 25 °C to 45 °C (Table 3). All the n>1 values indicated that the processes of sunflower torus-like MH adsorption of RB19 and ARS were favorable and homogeneous. ARS's Langmuir constant (K_L) was higher than that of RB19, and it was confirmed that the interaction between ARS and MH was stronger than that for RB19. As shown in Table 3, the adsorption capacities of MH increased from 349.85 to 410.21 mg/g for AR and from 231.78 to 338.24 mg/g for RB19 when the temperature increased from 25 °C to 45 °C. It was proven that the processes of sunflower torus-like MH microsphere particles adsorbing these dyes were endothermic. Under the same conditions, the saturated capacity of the MH adsorption of ARS was higher than that for RB19. This difference in the adsorption capacities of RB19 and ARS on sunflower torus-like MH might be related to the dyes' molecular structure.

The indispensable parameter of the maximum adsorption capacity (q_{max}) is used for evaluating the various adsorbents' performances and plays an important role in screening suitable adsorbents. In this study, the adsorbates and adsorption temperature conditions were chosen to compare performance and efficiency. The q_{max} values for the adsorption of RB19 and ARS dyes from different materials reported elsewhere are presented in Table 4. The analysis results indicate that the sunflower torus-like MH products have a satisfactory anthraquinone dye removal effect compared

Table 4. The q_{max} of RB19 and ARS on MH microsphere particles vs. different materials

Dyes	Adsorbent	q_{max} (mg/g)	Temperature (°C)	References
RB19	Iron rich Terra Rosa soil	4.11	25	[68]
RB19	Cucurbit[8] uril	714.29	25	[69]
RB19	Cucurbit[6] uril	100.50	25	[69]
RB19	Chitosan-Coated Magnetic Hydroxyapatite Nanoparticles	60.90	------	[70]
RB19	Whisker-shaped	43.48	25	This work
RB19	Lump-shaped	114.01	25	This work
RB19	Sunflower torus-like MH microsphere particles	231.78	25	This work
RB19	Sunflower torus-like MH microsphere particles	283.04	35	This work
RB19	Sunflower torus-like MH microsphere particles	338.24	45	This work
ARS	Vitis tree leaves	66.40	25	[71]
ARS	Magnetic chitosan	40.12	30	[72]
ARS	Termite hill	1.43	------	[73]
ARS	Nano gamma-alumina	54.40	------	[74]
ARS	Phenyl/amine end-capped tetraaniline	236.00	------	[53]
ARS	Hydrogel-Fungus Composites	31.30	25	[75]
ARS	Whisker-shaped	98.86	25	This work
ARS	Lump-shaped	151.34	25	This work
ARS	Sunflower torus-like MH microsphere particles	349.85	25	This work
ARS	Sunflower torus-like MH microsphere particles	382.41	35	This work
ARS	Sunflower torus-like MH microsphere particles	410.21	45	This work

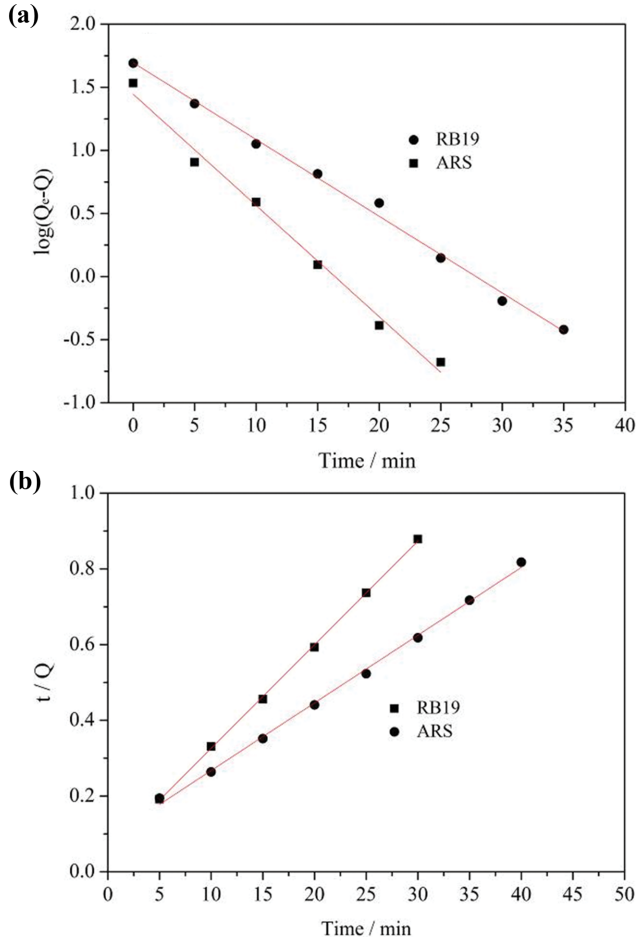

Fig. 17. Adsorption kinetics fitting curve. (a) Pseudo-first-order kinetic model, (b) pseudo-second-order kinetic model.

to the various adsorbents previously reported and various shapes of MH.

5. Adsorption Kinetics

The adsorption rate is one of the essential factors when assessing a new material to be used as an adsorbent. The pseudo-first and second-order kinetic models were implemented to investigate sunflower torus-like MH microsphere adsorption of the dyes. The adsorption kinetics for these anthraquinone dyes were fitted by pseudo-first-order and pseudo-second-order models. The adsorption kinetic fitting curves and parameters are shown in Fig. 17 and Table 5, respectively.

The applicability of the two kinetic models was comparatively analyzed by fitting graphs and correlation coefficients. Table 5 shows the results of sunflower torus-like MH microsphere adsorption of ARS; the correlation coefficients followed the order $R^2_{pso}>R^2_{pfo}$. This process was an imperfect fit with the pseudo-first-order model with a low correlation coefficient (0.9890). The low value indicated that the fitting with the pseudo-first-order model was not suitable. The pseudo-second-order model fitting had a high correlation coefficient of 0.9994. Moreover, the theoretical adsorption capacity (Q_m) value was closer to the experimental q_m. Hence, the analysis showed that the second-order kinetic model was a satisfactory candidate for describing the adsorption process of ARS on MH. For MH adsorption of RB19, the correlation coefficients of the two models were very similar, and R^2_{pso} was just slightly larger than R^2_{pfo}. However, the value of the theoretical adsorption capacity (Q_m) calculated by the pseudo-first-order model was closer to the experimental value (q_m) than that for the pseudo-second-order model. Therefore, the adsorption kinetics of RB19 onto the surface of sunflower torus-like MH microsphere particles were well defined by the pseudo-second-order model. As shown in Table 5, the uptake rates (K_1 and K_2) of ARS were higher than those for RB19. This result revealed that sunflower torus-like MH microsphere particles had a stronger surface affinity for ARS than for RB19. Consequently, adsorption kinetics may be dependent on adsorbent surface properties and the dyes' molecular structures.

6. Possible Adsorption Mechanism

The FT-IR and XPS analyses indicated that the adsorption capacity and mechanism were inconsistent in the process of removal ARS and RB19 from solution. After the same amount of adsorbent was treated with the same concentration of dye solution, the diffraction peaks of FT-IR and XPS were changed more significantly after adsorption of ARS. The high-resolution XPS spectra showed that the binding energy of magnesium atoms and oxygen atoms were changed. Thus, some chemical bond may be formed when dye molecules are adsorbed on the sunflower torus-like sample surface. The difference in the adsorption capacities between RB19 and ARS on the sunflower torus-like MH might be related to the dyes' molecular structure. Thus, the mechanism of MH dye adsorption may be related to the molecular structure of the dye. Consequently, the possible mechanism of the sunflower torus-like MH adsorption of RB19 (a) and ARS (b) is shown in Scheme 1. From Scheme 1(a), hydrogen bonds were formed between amino functional group hydrogen atoms or quinoid ring oxygen atoms in RB19 dye and the hydroxyl group oxygen atoms in sunflower torus-like MH. These bonds are believed to play quite an important role in the mechanism of sunflower torus-like MH adsorption of RB19. In contrast, OH groups were present in the benzenoid ring in Alizarin red S (ARS) dyes. Due to the special molecular structure, the OH groups in ARS molecules have weak acidity and can ionize hydrogen ions when ARS is in aqueous solution [52]. However, there was no significant change in the adsorption capacity when the pH of the ARS solution was changed between 4 and

Table 5. The adsorption kinetics data

Dyes	T (°C)	q_m (mg/g)	Pseudofirst-order model			Pseudosecond-order model		
			K_1 (min^{-1})	Q_m (mg/g)	R^2	K_2 (min^{-1})	Q_m (mg/g)	R^2
ARS	25	34.14	0.203	27.90	0.9890	0.0144	36.54	0.9994
RB19	25	49.18	0.136	47.16	0.9934	0.00396	55.01	0.9976

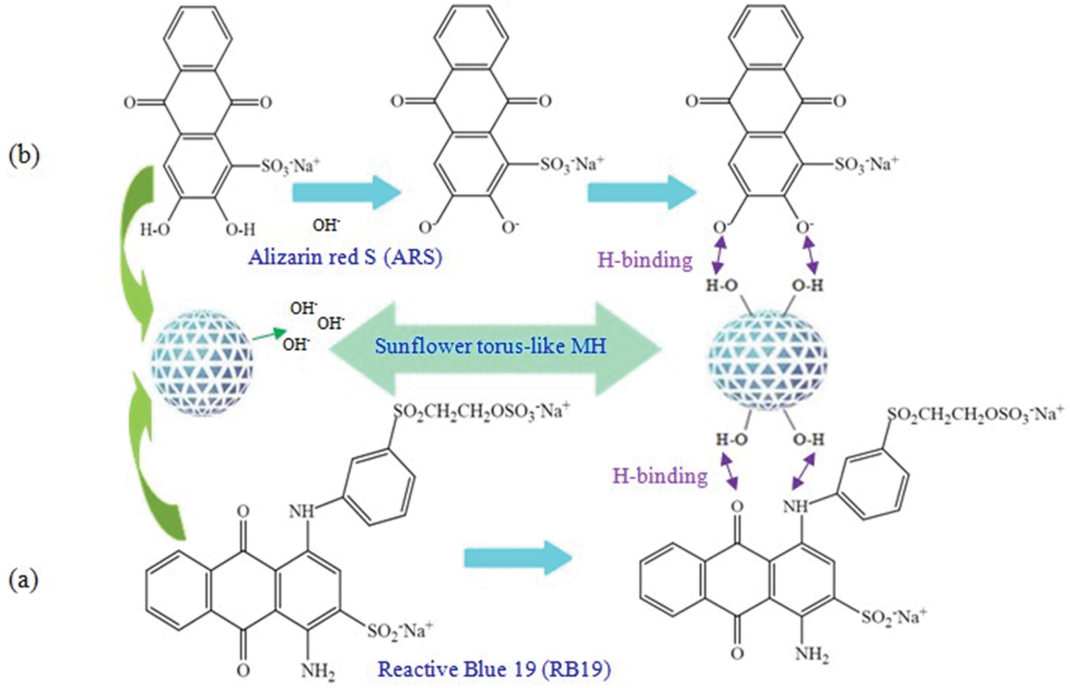

Scheme 1. Possible mechanism of the sunflower torus-like MH adsorption of RB19 (a) and ARS (b).

10. This result occurred because the hydroxide ions ionized from MH adjusted the solution pH value. Thus, the OH groups in ARS molecules reacted with the free hydroxide ions in solution first. Then, the ARS dyes were strongly adsorbed on the surface of the sunflower torus-like MH via the formation of hydrogen bond between the negatively charged oxygen atom of the quinoid ring in the molecule of ARS dyes and the hydroxyl group oxygen atoms in sunflower torus-like MH, as shown in Scheme 1(b).

CONCLUSION

Sunflower torus-like MH microsphere particles were prepared via a gentle and simple one-step method. The as-synthesized novel materials displayed abundant interstices and rough surfaces, resulting in high surface areas. The achievements of this investigation and analysis indicated that the MH microsphere is an effective purification material for absorbing ARS and RB19 from wastewater solutions. The purified supernatant was easily separated from the adsorbent carrying harmful substances. After the exposure of adsorbents to dye solutions, dye-loaded particles deposit at the bottom of the apparatus. The optimized adsorption process parameters were: adsorbent amount (25 mg for RB19 and 40 mg for ARS), contact time (30 min for RB19 and 20 min for ARS), adsorption temperature (25 °C), dye solution pH (4-10) and rotating speed (180 r/min). Dye removal rates were 91.65% and 83.03% for ARS and RB19, respectively. Various theoretical models were employed to calculate the adsorption kinetics and isotherms. The adsorption process of the MH microsphere adsorption of ARS obeyed the Freundlich model, and that of MH microsphere adsorption RB19 conformed to the Langmuir isotherm model. The kinetic adsorption experimental data of the dye adsorbed materials conformed to the pseudo-second-order model for ARS and to the pseudo-first-order model for RB19. The maximum adsorption capacity of the as-prepared MH microsphere was 349.85 mg/g and 231.78 mg/g for ARS and RB19, respectively, at 25 °C. As insights regarding MH as an eco-friendly and economic adsorbent, our results illustrate that the novel microsphere material has application potential as a high-performance regenerative treatment agent to remove dyes from polluted water. The analyses indicated that the RB19 and ARS dyes were absorbed on the surface of the sunflower torus-like MH via hydrogen bond formation.

ACKNOWLEDGEMENTS

This work was supported by the National Natural Science Foundation of China (21076131), the Science and Technology Research Program of Chongqing Municipal Education Commission (KJ1710245, KJ1710256, KJQN20181230, KJZD- K201801201 and KJQN201901208), and the Program of Chongqing Science and Technology Commission (cstc2018jcyjAX0813).

REFERENCES

1. A. Mohammadi, H. Daemi and M. Barikani, *Int. J. Biol. Macromol.*, **69**, 447 (2014).
2. M. A. A. Zaini, T. Y. Cher, M. Zakaria, M. J. Kamaruddin, S. H. M. Setapar and M. A. C. Yunus, *Desalin. Water. Treat.*, **52**, 3654 (2014).
3. X. H. Guan, P. Qu, X. Guan and G. S. Wang, *Rsc Adv.*, **4**, 15579 (2014).
4. A. Hassani, A. Khataee, S. Karaca, M. Karaca and M. Kiransan, *Chem. Eng. J.*, **3**, 2738 (2015).
5. M. Saranya, R. Ramachandran, E. J. J. Samuel, S. K. Jeong and

A. N. Grace, *Powder Technol.*, **279**, 209 (2015).
6. F. Hayeeye, M. Sattar, W. Chinpa and O. Sirichote, *Colloids Surf., A.*, **513**, 259 (2017).
7. A. Malathi and J. Madhavan, *J. Nano Res-SW.*, **48**, 49 (2017).
8. A. Muthukkumaran and K. Aravamudan, *J. Environ. Manage.*, **204**, 424 (2017).
9. Y. Huang, X. Zheng, S. Feng, Z. Guo and S. Liang, *Colloids Surf., A.*, **489**, 154 (2016).
10. A. U. Chaudhari, D. Paul, D. Dhotre and K. M. *Kodam, Water Res.*, **122**, 603 (2017).
11. W. J. Epolito, Y. H. Lee, L. A. Bottomley and S. G. Pavlostathis, *Dyes Pigm.*, **67**, 35 (2005).
12. M. Becelic-Tomin, B. Dalmacija, L. Rajic, D. Tomasevic, D. Kerkez, M. Watson and A. Prica, *Sci. World J.*, **2014**, 234654 (2014).
13. C. R. Holkar, A. B. Pandit and D. V. Pinjari, *Bioresour. Technol.*, **173**, 342 (2014).
14. E. R. A. Ferraz, M. D. Grando and D. P. Oliveira, *J. Hazard. Mater.*, **192**, 628 (2011).
15. M. Husain and Q. Husain, *Crit. Rev. Env. Sci. Technol.*, **38**, 1 (2008).
16. J. Lin, W. Ye, H. Zeng, H. Yang, J. Shen, S. Darvishmanesh, P. Luis, A. Sotto and B. Van der Bruggen, *J. Membr. Sci.*, **477**, 183 (2015).
17. A. K. Verma, R. R. Dash and P. Bhunia, *J. Environ. Manage.*, **93**, 154 (2012).
18. S. L. Stupar, B. N. Grgur, A. E. Onjia and D. Z. Mijin, *Int. J. Electrochem. Sci.*, **12**, 8564 (2017).
19. Z. M. Cui, Z. Chen, C. Y. Cao, L. Jiang and W. G. Song, *Chem. Commun.*, **49**, 2332 (2013).
20. S. Yuan, Y. Fan, Y. Zhang, M. Tong and P. Liao, *Environ. Sci. Technol.*, **45**, 8514 (2011).
21. J. Fu, Z. Chen, M. Wang, S. Liu, J. Zhang, J. Zhang, R. Han and Q. Xu, *Chem. Eng. J.*, **259**, 53 (2015).
22. Z. Hasan and S. H. Jhung, *J. Hazard. Mater.*, **283**, 329 (2015).
23. T. R. Das, S. Patra, R. Madhuri and P. K. Sharma, *J. Colloid Interface Sci.*, **509**, 82 (2018).
24. A. Paz, J. Carballo, M. Jose Perez and J. Manuel Dominguez, *Chemosphere*, **181**, 168 (2017).
25. C. N. Reddy, A. N. Kumar and S. V. Mohan, *J. Hazard. Mater.*, **343**, 49 (2018).
26. J. Zhang, Z. Xiong and X. S. Zhao, *J. Mater. Chem.*, **21**, 3634 (2011).
27. A. Malathi, P. Arunachalam, J. Madhavan, A. M. Al-Mayouf and M. A. Ghanem, *Colloids Surf., A.*, **537**, 435 (2018).
28. X. Li, W. Zhang, S. Lai, Y. Gan, J. Li, T. Ye, J. You, S. Wang, H. Chen, W. Deng, Y. Liu, W. Zhang and G. Xue, *Chem. Eng. J.*, **332**, 440 (2018).
29. V. Vimonses, S. Lei, B. Jin, C. W. K. Chowd and C. Saint, *Chem. Eng. J.*, **148**, 354 (2009).
30. L. Wang and A. Wang, *J. Hazard. Mater.*, **160**, 173 (2008).
31. M. K. Purkait, A. Maiti, S. DasGupta and S. De, *J. Hazard. Mater.*, **145**, 287 (2007).
32. B. Acevedo, R. P. Rocha, M. F. R. Pereira, J. L. Figueiredo and C. Barriocanal, *J. Colloid Interface Sci.*, **459**, 189 (2015).
33. F. Marrakchi, M. Bouaziz and B. H. Hameed, *Colloids Surf., A.*, **535**, 157 (2017).
34. C. C. dos Santos, R. Mouta, M. C. Castro Junior, S. A. Abreu Santana, H. A. dos Santos Silva and C. W. Brito Bezerra, *Carbohyd. Polym.*, **180**, 182 (2018).
35. K. Soleimani, A. D. Tehrani and M. Adeli, *Ecotoxicol. Environ. Saf.*, **147**, 34 (2018).
36. L. Lefebvre, G. Agusti, A. Bouzeggane and D. Edouard, *Catal. Today*, **301**, 98 (2018).
37. D. Zhao and X. Wu, *Mater. Lett.*, **210**, 354 (2018).
38. F. Sheng, X. Zhu, W. Wang, P. Wang and R. Zhang, *J. Chem. Soc-Taip.*, **64**, 1111 (2017).
39. Y. He, D. B. Jiang, J. Chen, D. Y. Jiang and Y. X. Zhang, *J. Colloid Interface Sci.*, **510**, 207 (2018).
40. K. Kuang, X. Huang and G. Liao, *Process Saf. Environ.*, **86**, 182 (2008).
41. R. Suihkonen, K. Nevalainen, O. Orell, M. Honkanen, L. Tang, H. Zhang, Z. Zhang and J. Vuorinen, *J. Mater. Sci.*, **47**, 1480 (2012).
42. Z. Wu, D. Pan, Z. Chen and Z. Lin, *Acta Chim. Sinica,* **70**, 2045 (2012).
43. W. Zou, L. Liu, H. Li and X. Han, *Korean J. Chem. Eng.*, **33**, 2073 (2016).
44. H. Li, S. Liu, J. Zhao and N. Feng, *Colloids Surf. A.*, **494**, 222 (2016).
45. J. Hao, C. Dai, Y. Liu and Q. Yang, *Desalin. Water. Treat.*, **90**, 252 (2017).
46. D. Jiang, Q. Yu, C. Huang, S. Chen, Y. Wu, J. Lin, J. Chen and P. Zhu, *J. Mol. Struct.*, **1175**, 858 (2019).
47. D. Jiang, Y. Yang, C. Huang, M. Huang, J. Chen, T. Rao and X. Ran, *J. Hazard. Mater.*, **373**, 131 (2019).
48. I. Langmuir, *J. Am. Chem. Soc.*, **38**, 2221 (1916).
49. H. Freundlich, *J. Phys. Chem.*, **57**, 385 (1906).
50. Y. S. Ho and G. McKay, *Process Biochem.*, **34**, 451 (1999).
51. A. Banaei, S. Samadi, S. Karimi, H. Vojoudi, E. Pourbasheer and A. Badiei, *Powder Technol.*, **319**, 60 (2017).
52. Y. D. Liang, Y. J. He, Y. H. Zhang and Q. Q. Zhu, *J. Environ. Chem. Eng.*, **6**, 416 (2018).
53. Y. Liu, J. Li, J. Zhu, W. Lyu, H. Xu, J. Feng and W. Yan, *Colloid. Polym. Sci.*, **296**, 1777 (2018).
54. W. Konicki, M. Aleksandrzak, D. Moszynski and E. Mijowska, *J. Colloid Interface Sci.*, **496**, 188 (2017).
55. J. Y. Yang, X. Y. Jiang, F. P. Jiao and J. G. Yu, *Appl. Surf. Sci.*, **436**, 198 (2018).
56. K. Gao, Q. Chang, B. Wang, N. Zhou and T. Qing, *Appl. Surf. Sci.*, **450**, 312 (2018).
57. X. Wang, L. Li, Z. H. Xie and G. Yu, *Electrochim. Acta*, **283**, 1845 (2018).
58. P. Casey, E. O'Connor, R. Long, B. Brennan, S. A. Krasnikov, D. O'Connell, P. K. Hurley and G. Hughes, *Microelectron. Eng.*, **86**, 1711 (2009).
59. D. Flahaut, M. Minvielle, A. Sambou, P. Lecour, C. Legens and J. Barbier, *Fuel,* **202**, 307 (2017).
60. S. Acharya, O. Trejo, A. Dadlani, J. Torgersen, F. Berto and F. Prinz, *Theor. Appl. Mech. Lett.*, **8**, 24 (2018).
61. S. Shoukat, H. N. Bhatti, M. Iqbal and S. Noreen, *Micropor. Mesopor. Mater.*, **239**, 180 (2017).
62. R. K. Ghosh and D. D. Reddy, *Water, Air, Soil Pollut.*, **224**, 1582 (2013).
63. K. Li, H. Li, T. Xiao, J. Long, G. Zhang, Y. Li, X. Liu, Z. Liang, F. Zheng and P. Zhang, *J. Environ. Manage.*, **251**, 109563 (2019).
64. H. J. Jang, S. B. Park, T. M. Bedair, M. K. Oh, D. J. Ahn, W. Park, Y. K. Joung and D. K. Han, *J. Ind. Eng. Chem.*, **59**, 266 (2018).

65. X. Sun and L. Xiang, *Mater. Chem. Phys.*, **109**, 381 (2008).
66. J. Lv, L. Qiu and B. Qu, *J. Cryst. Growth*, **267**, 676 (2004).
67. X. Hu, H. Zhang and Z. Sun, *Appl. Surf. Sci.*, **392**, 332 (2017).
68. D. Aktas, N. Dizge, H. C. Yatmaz, Y. Caliskan, Y. Ozay and A. Caputcu, *Water Sci. Technol.*, **76**, 3114 (2017).
69. X. Xie, X. Li, H. Luo, H. Lu, F. Chen and W. Li, *J. Phys. Chem. B.*, **120**, 4131 (2016).
70. N. Van Cuong and P. Quoc Hue, *Sci. World J.*, **2014**, 273082 (2014).
71. M. Bagtash and J. Zolgharnein, *J. Chemom.*, **32**, 2960 (2018).
72. L. Fan, Y. Zhang, X. Li, C. Luo, F. Lu and H. Qiu, *Colloids Surf., B.*, **91**, 250 (2012).
73. O. S. Ayanda, O. S. Amodu, H. Adubiaro, G. O. Olutona, O. T. Ebenezer, S. M. Nelana and E. B. Naidoo, *J. Water Reuse. Desal.*, **9**, 83 (2019).
74. J. Zolgharnein, N. Asanjrani, M. Bagtash and G. Azimi, *Spectrochim. Acta*, **126**, 291 (2014).
75. T. E. Dudu, D. Alpaslan, Y. Uzun and N. Aktas, *Int. J. Environ. Res.*, **11**, 557 (2017).